JMEPEG (2010) 19:467–480
DOI: 10.1007/s11665-010-9609-1
©ASM International
1059-9495/$19.00

Superplastic Response of Continuously Cast AZ31B Magnesium Sheet Alloys

J.M. Boileau, P.A. Friedman, D.Q. Houston, and S.G. Luckey

(Submitted December 8, 2009; in revised form January 4, 2010)

Magnesium sheet is typically produced for commercial applications with the traditional DC-ingot casting method. As a result of the hexagonal close-packed crystallographic structure in magnesium, multiple rolling passes and annealing steps are required to reduce the thickness of the ingots. Thus, high fabrication costs characterize the creation of magnesium sheet suitable for common forming operations. Recently, continuous casting (CC) technology, where molten metal is solidified directly into sheet form, has been applied to magnesium alloys; this method has shown the potential to significantly reduce the cost of fabricating magnesium sheet alloys. In order to understand the viability of the CC process, a study was conducted to investigate the superplastic potential of alloys produced by this method. This study focused on AZ31B Mg that was continuously-cast on twin-roll casters from three different suppliers. These three materials were compared with a production DC-cast AZ31B alloy in terms of microstructure, elevated-temperature tensile properties, and superplastic forming response. The data from this study found that microstructural features such as grain size and segregation can significantly affect the forming response. Additionally, the CC alloys can have equivalent or superior SPF response compared to DC-cast alloys, as demonstrated in both elevated temperature tensile tests and superplastic forming trials using a rectangular pan die.

Keywords cystallographic structure, formability, superplastic response

1. Introduction

The use of magnesium in automobiles has increased dramatically over the past twenty years. This is a result of magnesium's excellent strength-to-weight ratio as well as the push to reduce weight from vehicle structures. To date, application of magnesium has been mostly limited to castings; sheet applications have been limited by both the low formability and high cost of magnesium sheet. The low formability of magnesium sheet is a result of the crystallographic structure of magnesium; the hexagonally close-packed structure has an insufficient number of slip systems to allow for easy forming at room temperature. This significantly limits the use of conventional room-temperature stamping processes to economically form magnesium components in high volumes.

However, formability is improved when the temperature is increased. When magnesium is heated above 200 °C, thermal activation of pyramidal and prismatic slip planes occurs; this has been experimentally demonstrated to substantially improve formability (Ref 1). Thus, high-temperature forming processes like superplastic forming (SPF) can take advantage of the elevated temperature formability to form complex three-dimensional parts from magnesium sheet. SPF is typically accomplished by the gas forming of a heated sheet blank clamped between two die halves of a single-sided tool.

The crystallographic structure and corresponding low formability of magnesium also make the production of magnesium sheet expensive. The conventional production of magnesium sheet is based on the direct chill (DC) casting method. In this method, liquid metal is cast into large, thick molds and allowed to solidify into the form of ingots. After being scalped and homogenized, the ingot is fed into a primary mill and then a tandem mill. In these mills, the ingot is gradually reduced in thickness using large rollers. This massive gauge reduction requires significantly more rolling passes than other materials such as steel and aluminum; the limited number of slip systems in magnesium allows only a minimal amount of gauge reduction to be accomplished with each rolling pass. Additionally, rolling of magnesium requires off-line annealing steps between rolling passes. This is to reduce the strains introduced into the material and to achieve the total gauge reduction required to produce useable sheet. This is a very time and energy-intensive process that adds considerable cost to the final sheet product.

Continuous casting (CC) is an alternative, lower-cost process of producing magnesium sheet compared to DC-casting. Continuous casting has a smaller process inventory, quicker production rates, and is significantly less energy-intensive as compared to DC casting. In continuous casting, liquid metal is directly cast into a thin sheet of solidified metal approximately 5-25 mm in thickness and then fed directly into a series of rollers for reduction to the desired thickness. Thus, because the liquid metal is fed directly into a caster, the need for scalping, homogenizing, and a significant number of the expensive rolling passes is eliminated. Additionally, continuous casting results in

This article is based on a presentation at the AeroMat Conference, International Symposium on Superplasticity and Superplastic Forming (SPF) held in Austin, TX, June 23-26, 2008.

J.M. Boileau, P.A. Friedman, D.Q. Houston, and **S.G. Luckey**, Ford Research and Innovation Center, 2101 Village Road, Dearborn, MI 48121. Contact e-mail: pfriedma@ford.com.

a significantly faster solidification time compared to DC-casting. This produces a fine-grained microstructure with a refined precipitate structure that enhances the elevated temperature formability for processes such as SPF.

Compared to direct chill casting plants, continuous casting plants are much smaller in size, resulting in significantly lower investment costs. This also has the advantage of allowing the building of *specialty* cast houses that can economically manufacture a single product. Furthermore, the more direct processing route of continuous casting removes a large portion of the expensive conversion costs associated with thickness reduction. Thus, the lower investment and conversion costs, coupled with reduced production lead times, make continuous casting an attractive method of producing magnesium sheet for automotive applications. It has been estimated that continuous casting has the potential to reduce the cost of sheet magnesium to approximately $4.40 per kg ($2 per pound); at this level, it becomes an attractive material for vehicle lightweighting (Ref 2).

However, continuous casting production of magnesium sheet currently is a small-scale process. In addition, it is a significantly more complicated process compared to continuous casting of steel or aluminum. Casting of magnesium requires a protective atmosphere to prevent severe oxidation. The process controls for the creation of a consistently fine and equiaxed grain structure in production quantities are still under development. Additionally, quality concerns similar to those in the continuous casting of aluminum sheet exist; these include poor surface quality, microstructural segregation, crystallographic texture control, and gauge/profile control.

Therefore, in order to better understand the effect of processing on magnesium sheet formation, a mechanical and microstructural study was conducted. Three continuously cast alloys were examined and compared with the results from a commercially available DC alloy. While the specific details of each casting/rolling operation are proprietary to the respective supplier, the continuously cast alloys were all produced with a twin-roll caster. This process consists of solidifying molten magnesium directly between two large rolling wheels and allows for the direct coiling of as-cast magnesium for re-roll stock. Additional details and discussion on continuous casting methods are reviewed in Friedman (Ref 3).

2. Material for Study

AZ31 is an alloy composed primarily of magnesium alloyed with approximately 3% aluminum and 1% zinc. AZ31 is a commonly used wrought magnesium alloy, having reasonable mechanical properties and formability. These properties are a function of the alloying elements, the most important of which are detailed as follows (Ref 4, 5):

- *Aluminum* is the major alloying element in these alloys. Additions of aluminum increase the freezing range of Mg alloys, improving the fluidity of the metal during casting. In the solidified alloy, additions up to 10 wt.% aluminum increase the strength and hardness. In amounts greater than 6 wt.%, aluminum can also form a coarse, $Mg_{17}Al_{12}$-based incoherent precipitate upon heat-treatment; however, this precipitate adds little to the strength of the alloy. Consequently, many Mg-Al alloys are used in the as-cast or as-processed condition.
- *Zinc* is also a very important alloying element in Mg alloys. In general, zinc additions increase the strength at room temperature, especially in combination with aluminum. Additionally, when present with Zr, Th, or rare-earth elements, zinc additions can increase strength through the formation of precipitates upon heat-treatment. Zinc is often added to help improve the corrosion resistance of alloys containing Fe- or Ni-based impurities. However, care must be taken when alloying with zinc; in alloys where the amount of Zn is >1.5 wt.% and the amount of Al is >7 wt.%, hot shortness can result during casting and hot working.
- *Manganese* has a limited effect upon the strength of the Mg alloy. It is primarily added to improve the saltwater corrosion resistance of Mg alloys. This is accomplished through the formation of intermetallic compounds incorporating Fe, Ni, and other corrosion-promoting elements. In general, the amount of Mn added to an alloy is kept below 1.5 wt.%; in aluminum-containing alloys, the limit is restricted to 0.3 wt.%.
- *Rare Earth Elements* (such as Ce, La, Nd, and Pr) are added to increase the elevated temperature strength. They also reduce weld cracking and reduce the tendency for porosity in cast Mg alloys.
- *Zirconium* is a very powerful grain-refining element in Mg alloys containing Zn and rare-earth elements; amounts up to 3.8 wt.% are often added to these alloys. However, Zr cannot be used in Al-containing Mg alloys due to the formation of an Al-Zr intermetallic compound.
- *Iron, nickel, copper, and silicon* are generally undesirable impurities. These elements will significantly reduce the corrosion resistance of the Mg alloy. Most commercial alloys restrict these elements to levels of 0.05 wt.%; levels below 0.005 wt.% are often specified for high-performance, corrosion-resistant alloys. However, in certain alloys (like the ZC series), copper is often added in significant amounts for high-temperature strength. Similarly, Si is sometimes added to improve the fluidity of Mg in the molten state. However, in both these cases, the iron levels must be reduced to very low levels to prevent unacceptable corrosion rates from occurring.
- *Beryllium* is often added in very limited amounts (<0.001 wt.%) during the molten metal processing of the Mg alloy; these additions reduce the oxidation rate of the Mg at the surface of the metal. The amount used must be carefully controlled, as Be is a very strong grain coarsening agent.

A summary of the four AZ31 magnesium alloys used in this study, along with their gauge and tempers, is shown in Table 1. Throughout the remainder of this paper, the "code" name of the alloy will be used as identification.

3. Experimental Setup

3.1 Microscopy

To create the samples for grain size analysis, a sheet metal shear was used to create two samples for each of the four AZ31 alloys listed in Table 1. For each alloy, one sample was placed in a 500 °C furnace for 15 min; the other sample was left in the as-received condition. The samples were then sectioned and

mounted in the orientations shown in Fig. 1. The sections were polished using standard metallographic procedures through 0.05 μm colloidal silica; because the alloy was Mg, ethanol was used as the polishing coolant/lubricant in place of water. Following polishing, the samples were etched with an acetic-picral etch for ~20 s until the surface turned a brownish-tan in color.

The microstructures were examined using a Nikon Epiphot microscope; the grain sizes were quantified using the Image-ProPlus Image Analysis Software. The Minitab statistical software package was used to test for normalcy and statistical differences between the grain size data sets.

Samples for chemical analysis were also taken from each of the alloys. Chemical analysis was performed at Stork Climax Research Services (Wixom, MI) using Inductively-Coupled Plasma Emission Spectroscopy. Additionally, trace element analysis was performed on three of the alloys at Shiva Technologies (Syracuse, NY) using Glow Discharge Mass Spectroscopy. In both cases, the limit of accuracy of the compositional analysis is ±5% of the measured value.

3.2 Heat Treat Response

Prior to conducting superplastic tensile tests, a quick study was performed to ensure that the heat treatment time was adequate to fully anneal the alloys. Samples of the DC material were placed in a furnace at four different temperatures (300, 350, 400, and 450 °C) for times up to 120 min. Hardness measurements using a Knoop indenter were taken on the as-received material and the material after heat treatment.

Table 1 The AZ31 alloys examined in this study

Manufacturer code	Casting method	Temper	Gauge, mm
DC	Direct chill	O	1.60
CC-1	Continuously cast	O	3.20
CC-2	Continuously cast	H24 + soft annealed	1.45
CC-3	Continuously cast	H24	1.25

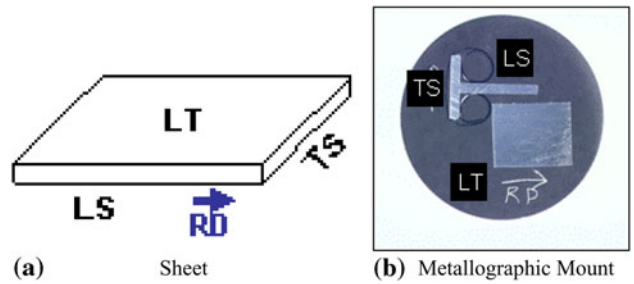

Fig. 1 Orientation of metallographic samples

3.3 Superplastic Tensile Tests

Superplastic tensile tests were conducted in a MTS Sintech machine (MTS Systems Corporation, Eden Prairie, MN). The load frame utilized an 8.9 kN (2000 lb) load cell; test control and data acquisition were performed using the MTS software. To reach the test temperature, the load frame was equipped with a three-zone split-furnace wrapped around specimen and pull rods. Tensile grips were manufactured from Inconel, a nickel-based super-alloy suitable for high-temperature applications. The tensile grips, shown with sample in Fig. 2(a), are designed to push on specimen shoulders (Fig. 2b) in opposite directions while squeezing specimen grip ends with blocks in an effort to contain grip material. The added benefit of these blocks is somewhat limited due to creep relaxation of grip load at the relatively high test temperatures. It has been shown that this type of design results in straining in grip regions, thus altering the desired strain rate condition (Ref 6). While control of strain rate is difficult, this technique offers a consistent method of characterizing superplastic sheet material.

Specimen temperature was monitored using thermocouples attached at both ends of the specimen gauge length and the temperature was maintained to within ±2 °C of the test temperature. Additional experimental details can be found in Friedman and Copple (Ref 7). Tensile tests were conducted at 425 °C at four different strain rates ranging from 5×10^{-4} s^{-1} to 5.0×10^{-3} s^{-1}.

3.4 Superplastic Forming Trials

Forming trials were conducted using an 800-ton production-level hydraulic superplastic forming press. The SPF die halves were secured to the upper and lower platens of the press; the forming gas source was connected to the lower die. The SPF press uses cartridge heaters within the upper and lower platens to conduct heat into the SPF die. Insulated doors allow the platens and SPF die to be fully enclosed and insulated. The doors are designed to raise and lower to allow sheets to be loaded and parts removed from between the die halves.

Target temperature for this set of experiments was 425 and 450 °C, which was a temperature range consistent with the test temperature applied in superplastic tensile tests. The tool temperature was monitored using two Type-K thermocouples embedded in each die half located within one inch of the

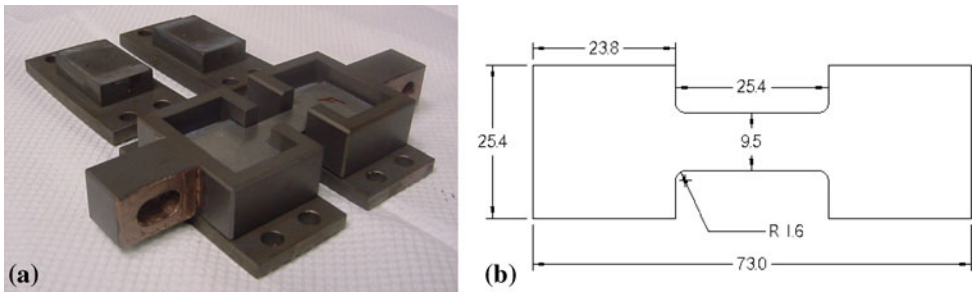

Fig. 2 (a) Photograph of the grips used for SPF tensile experiments and (b) schematic of the sample geometry (dimensions in mm)

forming surface. Temperature was recorded throughout the forming cycle using the die thermocouple and press data acquisition system. The average temperature of the die was maintained within ±5 °C of the target temperature.

Forming trials were conducted by placing a magnesium sheet blank between the die halves and closing the die; this applied a compressive force and created a gas-pressure seal around the outer perimeter of the blank. This seal allowed pressurized gas to be introduced into the lower die cavity and force the sheet into the forming cavity in the upper die. A pressure-versus-time curve was first predicted using LS-DYNA simulation. This curve was then programmed into the press control, which was capable of controlling to within ±2% of the target pressure.

Figure 3 shows the upper die half, which contained the forming cavity, of the single-sided SPF tool used in all forming trials. The single, deep cavity is a good geometry for comparing the forming limits of different magnesium sheet products. The rectangular cavity in Fig. 4 measured 600 mm in length, 400 mm in width, and 100 mm in depth. The die design also includes a 5° draft angle, 10 mm entry radii, and 20 mm plan radii. The depth of the die was fixed by a removable insert; at the bottom of the die, the insert made a 95° corner with the verticals walls of the cavity. To assess the formability of magnesium (detailed later in Sect 4.4), the bottom radius of a part formed in the cavity was allowed to be a function of the duration and magnitude of the gas pressure cycle.

Due to commercial limitations on available AZ31 Mg sheet width, only the DC and CC-3 sheet alloys were evaluated in the forming trials. Blanks were sheared to overall dimensions of 813 × 457 mm with respect to the longitudinal and transverse rolling directions. An alcohol wipe was used to remove the mill oil from each blank. Each blank was coated on both sides with a new proprietary Ford Motor Company SPF lubricant containing boron nitride prior to insertion in the SPF press.

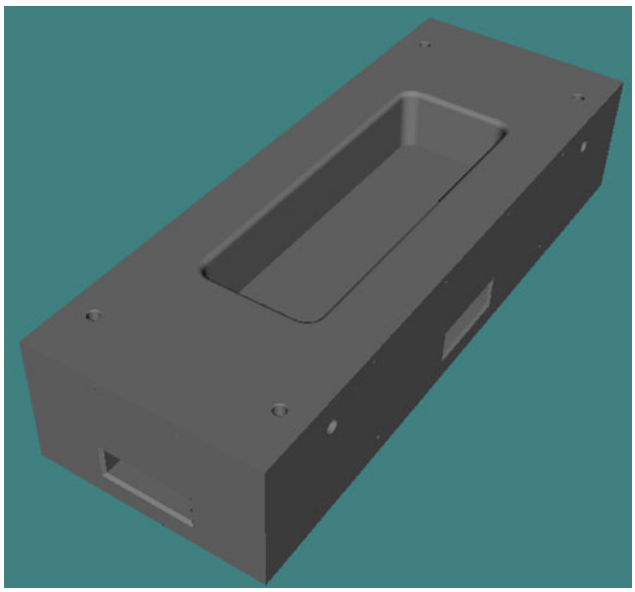

Fig. 3 The CAD model of the upper forming cavity of the rectangular SPF die

4. Results and Discussion

4.1 Metallurgical Analysis

4.1.1 Chemical Analysis. The results of the chemical analysis are shown in Table 2. All of the compositions are within the specified limits for the AZ31 alloy. Additionally, the table shows that all of the alloys have minimal levels of Si, Fe,

Table 2 Chemical composition of the AZ31 alloys examined in this study

	Chemical composition, wt.%				
Element	DC	CC-1	CC-2	CC-3	Range(a)
Al	3.24	2.87	3.16	3.18	2.5-3.5%
Zn	1.02	0.96	0.89	0.96	0.5-1.5%
Mn	0.45	0.36	0.31	0.35	0.2% min
Si	<0.01	0.02	0.01	0.02	…
Fe	0.01	<0.003	0.01	<0.003	0.03% max
Cu	<0.005	<0.005	<0.005	<0.005	0.05% max
Ni	<0.002	<0.002	<0.002	<0.002	0.03% max
Be	<0.0001	<0.0001	0.0005	0.0007	…

(a) Taken from ASM Mg and Mg alloys specialty handbook (Ref 4)

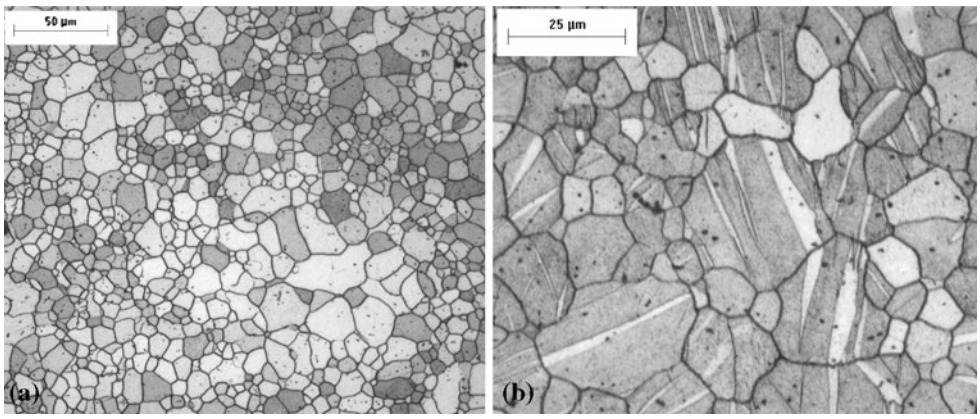

Fig. 4 Typical microstructural features observed in the AZ31 Mg alloys. Note that the light-colored acicular features in (b) are twins

Table 3 Trace element analysis of the AZ31 alloys

Element	Chemical composition, ppm by weight		
	DC	CC-1	CC-2
Pb	6.5	11	16
Zr	7.9	11	11
O	<10	<10	<10
Ce	0.25	0.37	8.2
Ca	0.51	1.3	1.1
Y	0.67	0.95	0.97
Sn	0.19	0.95	0.65
La	0.06	0.19	0.28
Nd	0.09	0.11	0.22
Ag	<0.05	0.08	0.12
Sb	0.05	0.09	0.12
Pr	0.04	0.03	0.09
Li	<0.005	0.34	0.04
Th	<0.01	<0.01	<0.01
Ti	0.03	<0.005	<0.005

Cu, and Ni; therefore, these alloys should have a high degree of resistance to corrosion. Table 3 presents the results of the trace element analysis of three AZ31 alloys. As this table shows, there are a large number of trace elements present. However, all of these elements are present in very low levels. Thus, the trace elements are not thought to have had any significant effect on the tensile and forming results of the AZ31 alloys detailed later in this report.

4.1.2 Microstructure. Figure 4 shows the typical microstructure observed in the AZ31 alloys. In general, the microstructure consists of a primary Mg-Al-Zn eutectic phase and a small number of randomly dispersed dark particles. The eutectic phase showed a variety of sizes and morphologies; additionally, as Fig. 4(b) shows, significant twinning was observed as well. The dark particles were not specifically determined; according to the literature, they are most probably either fragments of $Mg_{17}Al_{12}$ particles or of a manganese-aluminum phase. No evidence of any other phases (such as a Mg-Al-Zn ternary phase) was observed.

The Appendix details the microstructures of the four AZ31 alloys listed in Table 1. For each alloy, photomicrographs are presented in the three orientations for samples that are in the as-received conditions and the 500 °C/15 min heat treatment. A comparison of the four alloys found that differences do exist between the microstructures.

As a comparison of Fig. A1 and A2 shows, the DC material has a finer grain size in the as-received condition compared to the heat-treated condition. With one exception, both microstructures showed evidence of significant twinning. It was observed that the microstructure in the TS plane for the samples given the 500 °C/15 min heat treatment did not show much twinning. This is most probably due to the fact that these twins developed during the rolling process and therefore are predominantly in response to the elongation in that direction.

The as-received CC-1 material (Fig. A3) showed a wider range in the grain size (>70-150 μm) in the three orientations compared to the range seen for the heat-treated material (50-70 μm) (Fig. A4). This rather large distribution in grain size can have deleterious effects on the SPF response. This is due to the fact that grain boundary sliding is the controlling deformation mechanism in SPF. Work by Ghosh and Raj (Ref 8) has shown that a large distribution in grain size can result in premature fracture during superplastic deformation of certain alloys. Additionally, both microstructures showed evidence of significant twinning in the LT and LS orientations; the microstructures in the TS plane for both sets of samples did not show much twinning. Further, the microstructural examination observed evidence of center-line segregation along the rolling direction (LS). This is a common occurrence in continuously cast alloys since the center of the strip is the last to solidify during the casting process. This agglomeration of intermetallic particles can cause a significant directional effect in the alloy as well as limit the superplastic response of the material.

The CC-2 material (Fig. A5 and A6) was found to have a very fine grain size (20-30 μm) in the as-received condition and to experience only a modest amount of growth in grain size (25-60 μm) during the heat treatment. However, the material exhibits significant center-line segregation along the LS rolling direction. As seen previously, both CC-2 microstructures showed evidence of significant twinning only in the LT and LS orientations; the microstructures in the TS plane did not show much twinning.

The CC-3 material (Fig. A7 and A8) exhibits a very fine grain size with a few extremely large grains in the microstructure (as noted in the maximums of the measured grain sizes). These very large grains are of concern because they inhibit grain boundary sliding; thus, these very large grains can cause early failure during superplastic deformation. Additionally, unlike the three previously examined alloys, the CC-3 alloy showed very limited twinning in the LT and LS orientations in the as-received condition (Fig. A7). This alloy did not show any evidence of twins after heat treatment (Fig. A8).

4.1.3 Grain Size. The quantification of the grain size in each of the AZ31 Mg alloys is shown in Fig. 5 and summarized in Table 4 and 5. (The Appendix presents detailed results for each of the alloys.) In general, several samples from each alloy were quantified and compared for each specific manufacturer and condition. No significant differences were observed within each set. Therefore, the grain size data presented in Fig. 5 and Table 4 and 5 can be considered typical of the grain sizes present within each of the alloys examined in this study.

The grain size data reveals four trends. First, the average grain size in all of the alloys is very fine (Fig. 5 and Table 4); further, the grains are slightly elongated in shape (Table 5). Both of these indicate that the Mg alloys in the as-received condition have been heavily cold-worked.

Second, the average grain size increases when the as-received Mg samples are given the 500 °C heat treatment for 15 min. The degree of this change varies greatly from alloy to alloy, with the CC-1 material showing the least change (~26%) and the DC material showing the greatest change (~79%.) This difference in grain size increase is believed to be due to different levels of strain introduced into the alloys. Each alloy was cold-worked to a different degree by the individual manufacturer. The high change associated with the DC material is consistent with the high amount of rolling employed in the DC process. Third, the range in grain sizes between different alloys is highly variable. Fourth, the range in grain sizes between the as-received and heat-treated samples of the same alloy also has a high degree of variability, with the heat-treated sample having a larger range than that seen in the as-received sample.

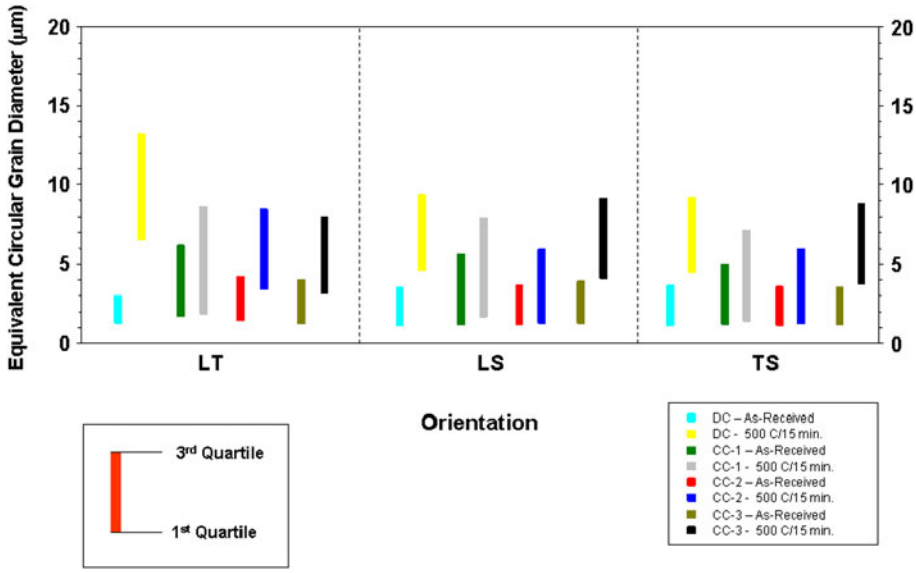

Fig. 5 Comparison of grain sizes in the AZ31 magnesium alloys

Table 4 Median grain sizes in the AZ31 magnesium alloys

		Median grain size (µm) for the orientation of:		
Manufacturer	**Condition**	**LT**	**LS**	**TS**
DC	As-received	1.98	2.05	2.03
	500 °C/15 min	9.56	6.67	6.45
CC-1	As-received	3.58	2.20	2.62
	500 °C/15 min	4.84	4.12	3.40
CC-2	As-received	2.53	2.11	2.06
	500 °C/15 min	5.54	2.92	2.82
CC-3	As-received	2.33	2.35	2.05
	500 °C/15 min	5.22	6.25	5.84

Table 5 Median grain aspect ratios of the AZ31 magnesium alloys

		Median aspect ratio(a) for the orientation of:		
Manufacturer	**Condition**	**LT**	**LS**	**TS**
DC	As-received	2.03	1.70	1.87
	500 °C/15 min	1.42	1.64	1.81
CC-1	As-received	1.60	1.89	1.98
	500 °C/15 min	1.55	1.77	1.99
CC-2	As-received	1.53	1.69	1.75
	500 °C/15 min	1.44	1.96	2.18
CC-3	As-received	1.74	1.72	1.74
	500 °C/15 min	1.45	1.45	1.47

(a) Defined as maximum diameter/minimum diameter (a circle has an aspect ratio of 1)

4.2 Heat-Treatment Response

The results of the effect of time and temperature on the hardness of the DC material are shown in Fig. 6. As this figure illustrates, the DC material is fully annealed after 5 min at 300 °C. Hence, it appears that longer exposure times at a given temperature do not significantly affect the hardness. Similarly, it appears that, for a given exposure time, higher temperatures also do not significantly affect the hardness.

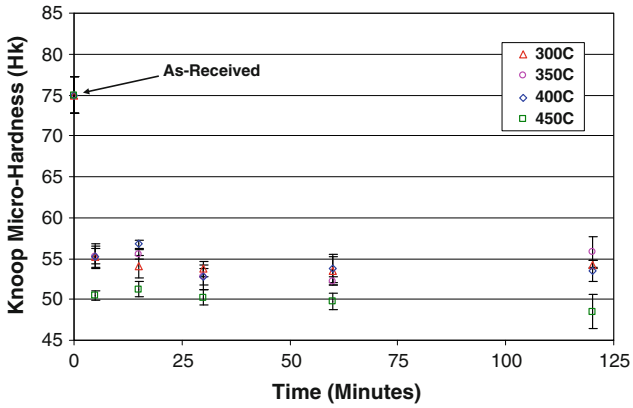

Fig. 6 The effect of temperature and time on the hardness of the DC-1 AZ31 Mg alloy received in the H24 temper. Note that the error bars represent ±1 SD

Because of the similarities in chemical composition and grain size amongst all four of the AZ31 alloys, the DC results can be extrapolated for the remaining three alloys. Thus, a heat treatment of at least 300 °C for at least 5 min will tend to completely anneal AZ31 in the as-received (or cold-rolled) condition.

4.3 Superplastic Tensile Tests

4.3.1 Elongation to Failure. Figure 7 presents the elongation-to-failure results for the four test materials as a function of initial strain rate. These results show that there is a high degree of correlation between elongation and deformation rate; the overall trend is that increasing the strain rate yields a

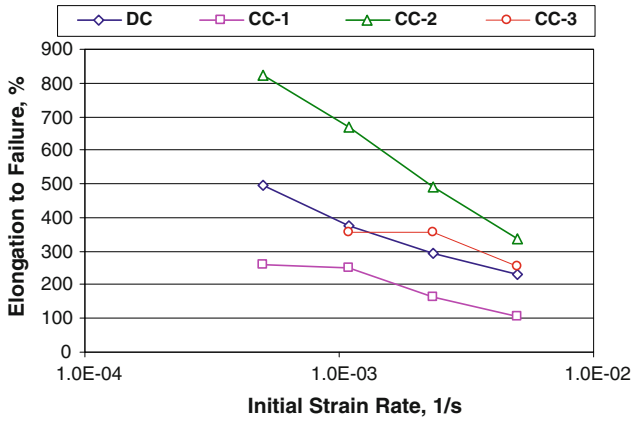

Fig. 7 The effect of initial strain rate on the elongation-to-failure in AZ31B Mg. Testing conducted at 425 °C on samples oriented parallel to the rolling direction

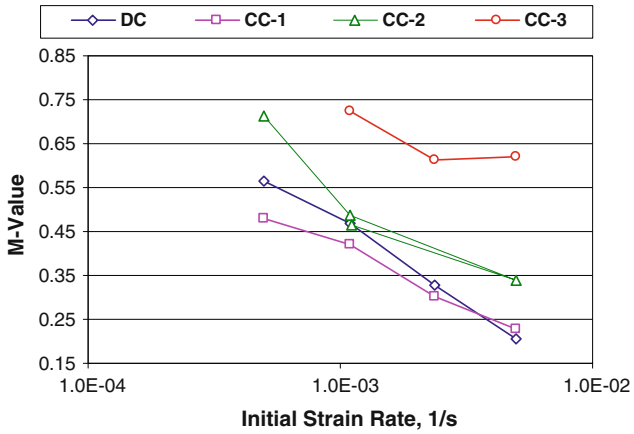

Fig. 8 Strain rate sensitivity (*m*-value) as a function of initial strain rate for AZ31B Mg. Tests conducted at 425 °C on samples oriented parallel to the rolling direction

lower elongation-to-failure. This loss of ductility is especially dramatic for the CC-2 material. In this case, the material displays greater than 800% elongation at the slowest strain rate of 5×10^{-4} s^{-1}; however, the elongation drops significantly (to approximately 350%) as the strain rate increases to 5×10^{-3} s^{-1}. Similarly, the DC and CC-3 materials both show a decrease in elongation-to-failure (500-250%) as the strain rate increases by an order of magnitude (Fig. 7). Further, the CC-1 material showed the same trend; however, the magnitude of the change was low, with elongation-to-failure values ranging from 250% to just over 100%.

The elongation results can be related to the microstructures present in each of the alloys. The greatest elongation-to-failure values were obtained from the CC-2 material; this can be directly attributed to the finer and more equiaxed grain structure present in the as-received condition. Since the primary rate-controlling mechanism during superplastic deformation is grain boundary sliding, the greater the grain boundary area, the greater the elongation that can arise.

The rather poor SPF response from the CC-1 material can be attributed to the large distribution in grain size. As illustrated in Fig. A3 and A4, this material has regions of coarse grains (with significant twinning) adjacent to very fine grain clusters. This type of grain size distribution inhibits the SPF response since it prevents efficient grain boundary sliding. In this case, the dominant deformation mechanism becomes thermally assisted dislocation motion and twinning; these mechanisms are not as sensitive to the rate of deformation. This may also explain why the elongation-to-failure results in the CC-1 material are relatively insensitive to strain rate (Fig. 7).

4.3.2 Strain-Rate Sensitivity. An important parameter for characterizing a superplastic material is the strain-rate sensitivity (*m*-value) of the material as a function of temperature and strain rate. For this analysis, the strain rates during the tensile tests were doubled at 5% strain to determine the rate sensitivity (*m*-value). The strain rate sensitivity was calculated using Eq 1:

$$m = \left(\frac{\log(P_2/P_1)}{\log(\dot{\varepsilon}_2/\dot{\varepsilon}_1)} \right) \quad \text{(Eq 1)}$$

where P_1 and P_2 are the flow stresses and $\dot{\varepsilon}_1$ and $\dot{\varepsilon}_2$ are the corresponding instantaneous strain rates before and after the applied jump in strain rate, respectively. For additional details on this test, see Friedman and Copple (Ref 7).

The data from the strain-rate sensitivity analysis are shown in Fig. 8. Similar to the elongation to failure data, the strain rate sensitivity (or *m*-value) decreases rapidly with increases in strain rate. Since a high strain rate sensitivity value can delay localized necking and improve superplastic response, these results are not unexpected. This is clearly the case for the CC-2 material; as Fig. 8 details, this alloy experiences a drop from over 0.7 at the slowest rate to under 0.35 at the fastest. While most of the alloys had a reasonable correlation between strain-rate sensitivity and elongation-to-failure, there was an exception. In the CC-3 material, the very high *m*-values do not correlate with the data for elongation to failure. At this time, the root cause for this case has not been determined; additional research is needed to understand the failure mechanism(s) in this alloy.

4.3.3 Orientation. A brief investigation into the effect of orientation was also conducted on the four Mg alloys listed in Table 1. Tensile samples were prepared in two orientations: tensile axis parallel to the rolling direction (L); and tensile axis transverse to the rolling direction (T). All of the tests were conducted at an initial strain rate of 1.1×10^{-3} s^{-1} and a temperature of 425 °C.

The elongation-to-failure results for the four materials are shown in Fig. 9. As this figure illustrates, there is a large effect of orientation for the CC-2 material; the elongation-to-failure data for the remaining three alloys show only a minor effect.

Figure 9 shows an interesting result when the tensile axis is transverse to the rolling direction (T); in this case, the elongation-to-failure value for the CC-2 material is similar to values for the CC-3 and DC materials. However, as shown in Fig. 10, this dramatic difference in elongation-to-failure cannot be explained by a significant difference in strain-rate sensitivity (*m*-value).

As Fig. 10 details, orientation does not appear to have a large effect on *m*-value. It is possible that this lower elongation-to-failure in the transverse direction (tensile axis perpendicular to the rolling direction) is a result of center-line segregation like that illustrated in Fig. A6. The segregation, extending across a large portion of the cross-sectional area, may inhibit grain boundary sliding in a large percentage of the grains. This could

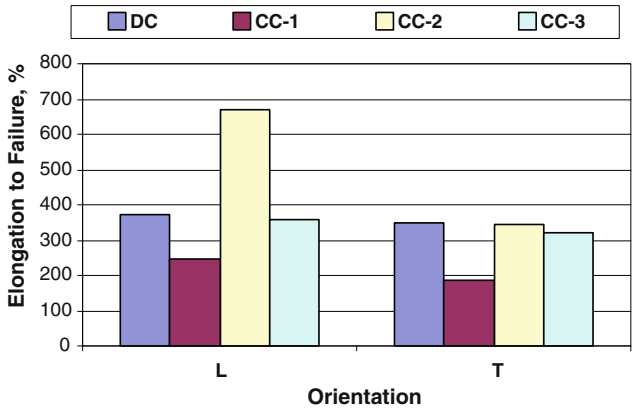

Fig. 9 The effect of sample orientation on the elongation-to-failure in AZ31B Mg. Testing conducted at 425 °C on samples orientated with the tensile axis parallel to the rolling direction (L) and transverse to the rolling direction (T) at an initial strain rate of 1.1×10^{-3} s^{-1}

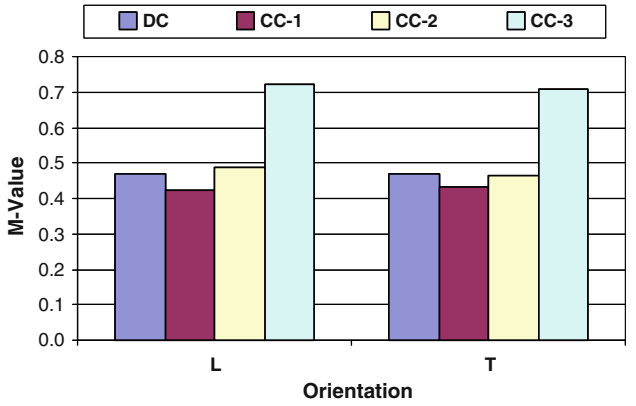

Fig. 10 Strain rate sensitivity (*m*-value) as a function of material and sample orientation for AZ31 Mg. Tests conducted at 425 °C for samples orientated with the tensile axis parallel to the rolling direction (L) and transverse to the rolling direction (T); initial strain rate = 1.1×10^{-3} s^{-1}

lead to failure at the observed lower elongation values. In the longitudinal direction (tensile axis parallel to the rolling direction), this segregation may occupy a much lower percentage of the available cross-sectional area. Thus, the segregation will not have the same effect since a higher percentage of the grains can easily slide past one another.

4.4 Forming Trial Results

To assess the sheet formability of the test alloys, forming trials were conducted using the equipment and die described in Sect 3.4 and shown in Fig. 3; Table 6 details the test parameters used in these trials. Due to the limited availability of AZ31 sheet that could meet the minimum blank size requirements of the die, only two of the AZ31 alloys (the DC and CC-3 materials) could be used for forming trials. In addition, due to limitations on the amount of sheet available, only two forming trials could be conducted for each of the conditions listed in Table 6. Although the small experimental sample size prevents statistical conclusions from being drawn, these trials allowed

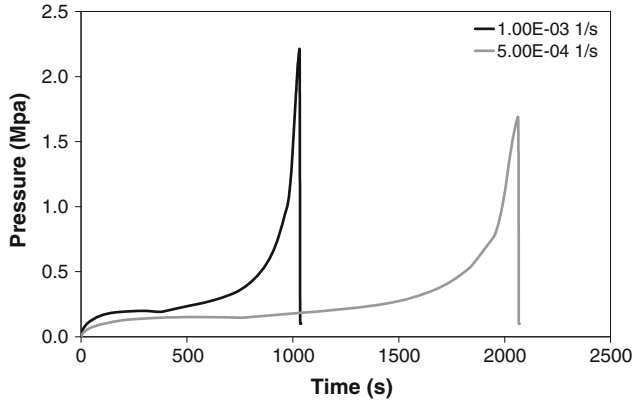

Fig. 11 Pressure vs. time cycle curves for the forming of magnesium sheet at target strain rates of 5×10^{-3} and 10^{-3} s^{-1} at a temperature of 425 °C

Table 6 Forming parameters applied to form the sheet magnesium within the superplastic forming die cavity

Supplier	Target strain rate, s^{-1}	Forming temperature, °C
DC	0.0005	425
	0.0005	450
CC-3	0.001	425
	0.0005	450
	0.001	450

preliminary trends to be established; these trends will be useful in guiding more extensive formability analyses in the future.

All panels were formed by applying the gas pressure cycles shown in Fig. 11. Each curve was developed using finite element analysis to control the forming rate of the sheet throughout the cycle at the target strain rates of 5×10^{-3} and 10^{-3} s^{-1}, respectively (Ref 9). Forming was carried out at two temperatures, 425 and 450 °C. It should be noted that the pressure curves in Fig. 11 were developed for forming the sheet at 425 °C. For the forming trials at 450 °C, these curves were then scaled to account for the decrease in sheet flow stress at this temperature.

Using the die geometry shown in Fig. 3, each forming trial was conducted until failure occurred with a rupture of the sheet; the rupture was due to one of two possible failure modes:

- Early cycle failure at the entry radius (Fig. 12a); or
- Failure in the bottom corner of the geometry once the cavity was fully formed (Fig. 12b).

Both the DC and CC-3 materials were fully formed at both target temperatures (425 and 450 °C) using the 5×10^{-3} s^{-1} pressure cycle. The failure mode for each alloy was a bi-axial failure in the bottom corner of the fully formed panel (like that shown in Fig. 12b). For the faster pressure cycle, which maintained a strain rate of 10^{-3} s^{-1}, the DC alloy failed very early in the forming cycle at the entry radius (like that shown in Fig. 12a). The entry radius is a region of the panel dominated by plane strain; thus, this type failure signifies that, for faster strain rates, the reduced level of rate sensitivity severely limits the complexity of shapes that can be formed with the sheet.

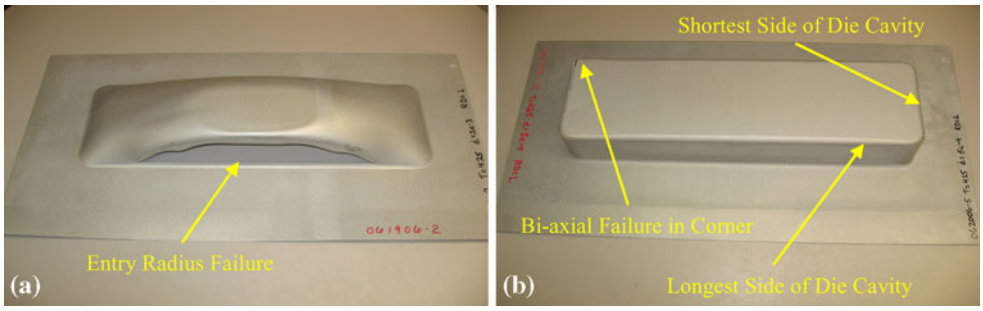

Fig. 12 Photographs of formed parts from the cavity die showing typical failure at (a) the entry radius of die cavity and (b) the bottom corner of the panel (Ref 9)

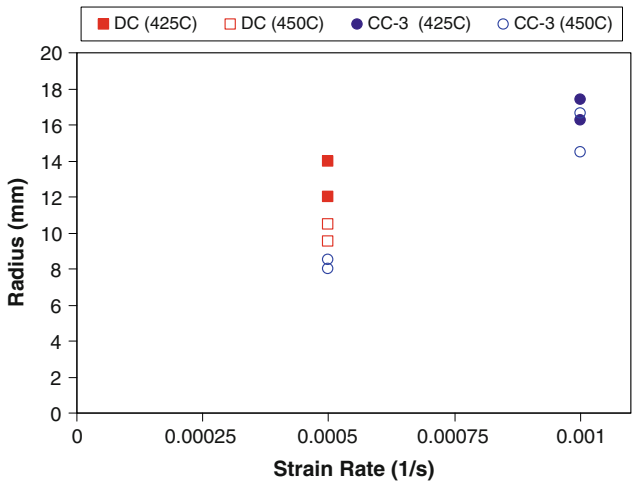

Fig. 13 Comparison of the bottom panel radii for the DC and CC-3 sheet alloys as a function of forming cycle strain rate and temperature

The CC-3 material was successfully formed with the 10^{-3} s^{-1} pressure cycle; for this material, failure occurred at the bottom corner (Fig. 12b) irrespective of the applied temperature. Higher-rate forming cycles were attempted with the CC-3 material; however, this induced failure at the entry radius (Fig. 12a) and prevented the forming of the cavity geometry.

The results of the forming trials show that the failure mode changes from the entry radius to biaxial fracture in the bottom corner with decreasing strain rate in both materials. Thus, this represents an increase in general sheet formability. Additionally, while these forming trials suggest that both materials could have been fully formed at slower strain rates ($< 5 \times 10^{-3}$ s^{-1}), the lengthy forming cycles required for this are considered impractical.

An additional assessment on the formability of each material was made by considering the effect of strain rate and temperature on the mid-point bottom radii achieved along both the short and long sides of the parts (Fig. 12b). The tighter the radius, the further the sheet had been driven into the cavity before the bi-axial corner failure. Therefore, the gas-formed radius data shown in Fig. 13 represent an indirect measure of sheet formability; additionally, it offers practical insight into a material's ability to conform to geometric details during stretch forming. From the limited data shown in Fig. 13, several general trends can be observed. First, the results do indicate that, for a strain rate of 5×10^{-3} s^{-1}, the CC-3 sheet can achieve a slightly smaller radius than the DC alloy. Second, it can also be observed that, with increasing strain rate, the final radii for the CC-3 material appear to increase. This increase in radius size likely represents a decrease in formability in the CC-3 alloy due to increased strain rate. Third, no clear trends can be drawn on the influence of temperature on formability.

Based on these results, it has been observed that the formability of each of the magnesium sheet alloys decreases with increasing forming strain rate; this also correlates with the tensile test results discussed previously in Sect 4.3. From analyzing the failure mode and the final radii (as a function of strain rate), the CC-3 material appeared to demonstrate slightly better formability than the DC alloy for an equivalent forming-cycle strain rate. Further, the CC-3 sheet material was capable of forming the geometry at a higher strain rate, reducing by half the forming time compared to the DC sheet. This improvement in formability of the CC-3 material is consistent with the SPF tensile results; as shown previously in Fig. 8, the tensile results indicated a higher strain rate sensitivity value for the CC-3 material as compared to the DC material.

5. Summary and Conclusions

In this study, three AZ31B alloys produced by twin-roll continuous casting were studied and compared to a commercially available, DC ingot-produced AZ31B alloy. This study focused on examining the microstructural features and the superplastic response of the four AZ31B alloys. The data indicate that AZ31B magnesium alloys fabricated with the continuous casting method can have properties equivalent to (and potentially superior to) AZ31B alloys fabricated with the DC-ingot method.

The results of this study allow the following specific conclusions to be drawn:

- The microstructures of the four AZ31B alloys had significant differences. The grain sizes showed considerable variation, both in size between the alloys and in the range of sizes within a particular alloy. In general, the alloys with lower variations in grain size range yielded better SPF responses.
- The microstructures of the four AZ31B alloys showed significant twinning in the LS (rolling × thickness) and LT (rolling × transverse to rolling) orientations regardless of the condition of the material (as-received or heat-treated). Annealing did reduce the presence of twinning in the TS orientation.

- All four of the AZ31B alloys showed a reduction in elongation-to-failure as the strain rate was increased during elevated temperature tensile tests. The degree of this reduction varied between the alloys but was consistent with a similar correlation between strain rate sensitivity and strain rate.
- The CC alloys showed evidence of center-line segregation. This was probably the cause for the lower elongation-to-failure values observed in samples having the tensile axis oriented transverse to the rolling direction.
- The elevated temperature tensile tests and superplastic forming trials using a rectangular pan die demonstrate that the CC alloys can have equivalent or superior SPF response compared to DC-cast alloys.

Appendix: Individual Photographs and Measurements of the Grain Size in the AZ31 Alloy Sheet Samples Examined in this Study

Note: Orientations are designated as follows:

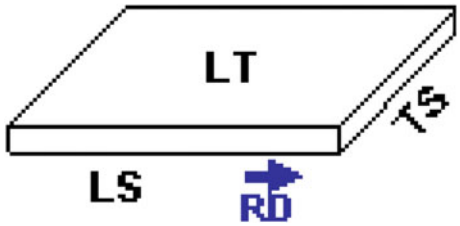

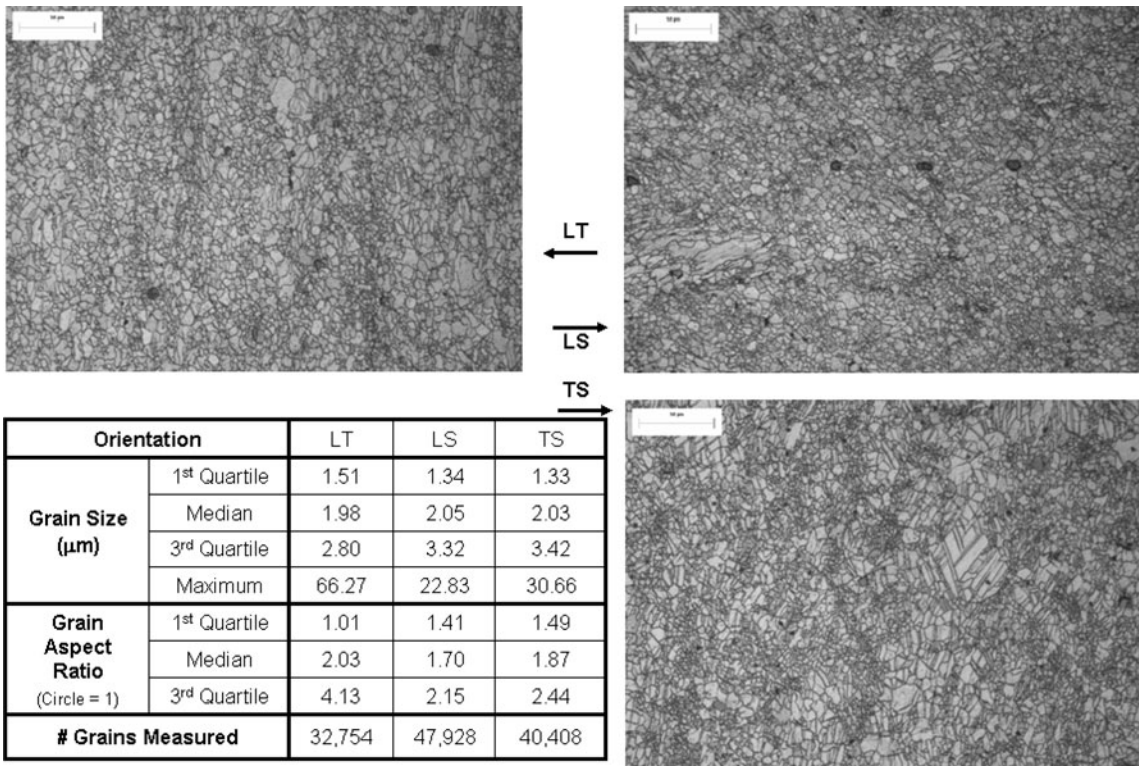

Orientation		LT	LS	TS
Grain Size (μm)	1st Quartile	1.51	1.34	1.33
	Median	1.98	2.05	2.03
	3rd Quartile	2.80	3.32	3.42
	Maximum	66.27	22.83	30.66
Grain Aspect Ratio (Circle = 1)	1st Quartile	1.01	1.41	1.49
	Median	2.03	1.70	1.87
	3rd Quartile	4.13	2.15	2.44
# Grains Measured		32,754	47,928	40,408

Fig. A1 Grain size observed in the DC alloy (as-received condition)

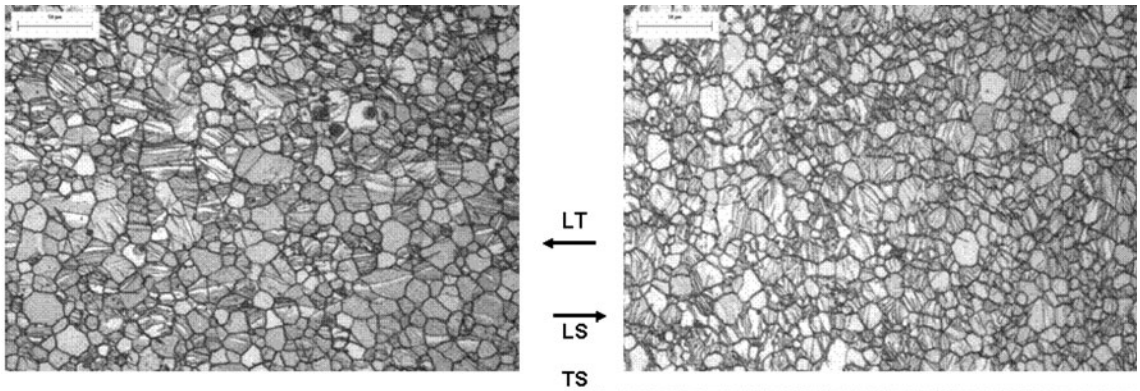

Orientation		LT	LS	TS
Grain Size (μm)	1st Quartile	6.81	4.82	4.72
	Median	9.56	6.67	6.45
	3rd Quartile	12.96	9.09	8.94
	Maximum	66.25	37.79	51.01
Grain Aspect Ratio (Circle = 1)	1st Quartile	1.25	1.34	1.42
	Median	1.42	1.64	1.81
	3rd Quartile	1.70	2.13	2.55
# Grains Measured		4666	6513	6181

Fig. A2 Grain size observed in the DC alloy (heat treated for 15 min at 500 °C)

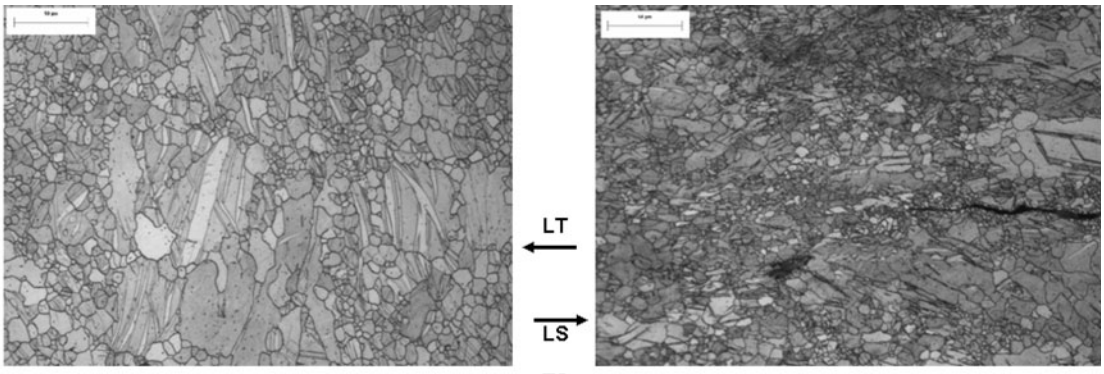

Orientation		LT	LS	TS
Grain Size (μm)	1st Quartile	1.96	1.39	1.47
	Median	3.58	2.20	2.62
	3rd Quartile	5.97	5.40	4.76
	Maximum	153.64	72.20	66.16
Grain Aspect Ratio (Circle = 1)	1st Quartile	1.34	1.49	1.51
	Median	1.60	1.89	1.98
	3rd Quartile	2.01	2.56	2.92
# Grains Measured		15,769	25,091	20,001

Fig. A3 Grain size observed in the CC-1 alloy (as-received condition)

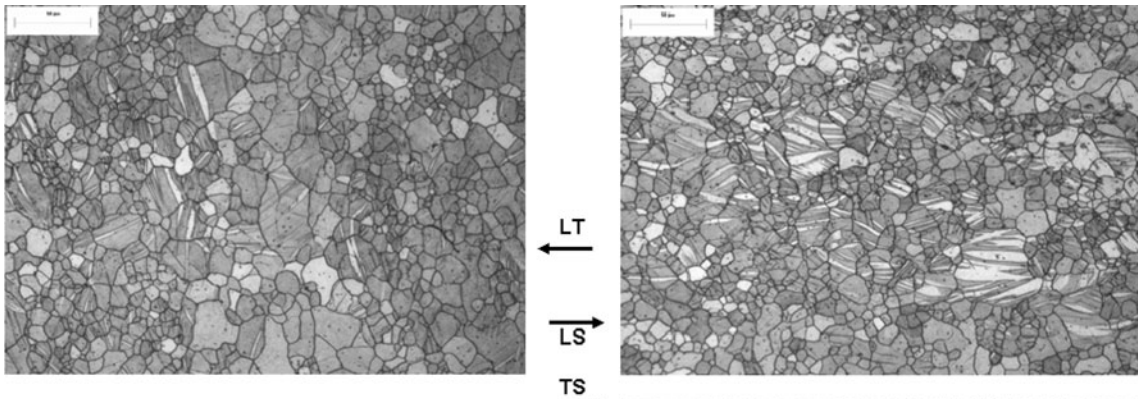

Orientation		LT	LS	TS
Grain Size (μm)	1st Quartile	2.10	1.90	1.63
	Median	4.84	4.12	3.40
	3rd Quartile	8.37	7.71	6.88
	Maximum	51.86	67.85	70.21
Grain Aspect Ratio (Circle = 1)	1st Quartile	1.31	1.41	1.51
	Median	1.55	1.77	1.99
	3rd Quartile	1.94	2.44	3.00
# Grains Measured		11,403	10,676	10,798

Fig. A4 Grain size observed in the CC-1 alloy (heat treated for 15 min at 500 °C)

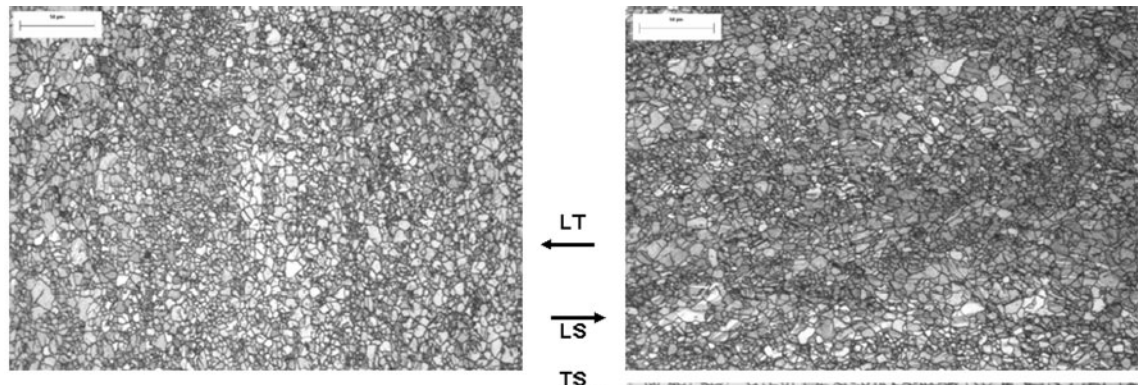

Orientation		LT	LS	TS
Grain Size (μm)	1st Quartile	1.62	1.40	1.38
	Median	2.53	2.11	2.06
	3rd Quartile	3.93	3.41	3.34
	Maximum	22.92	30.68	26.74
Grain Aspect Ratio (Circle = 1)	1st Quartile	1.30	1.40	1.42
	Median	1.53	1.69	1.75
	3rd Quartile	1.86	2.15	2.29
# Grains Measured		43,326	36,651	45,084

Fig. A5 Grain size observed in the CC-2 alloy (as-received condition)

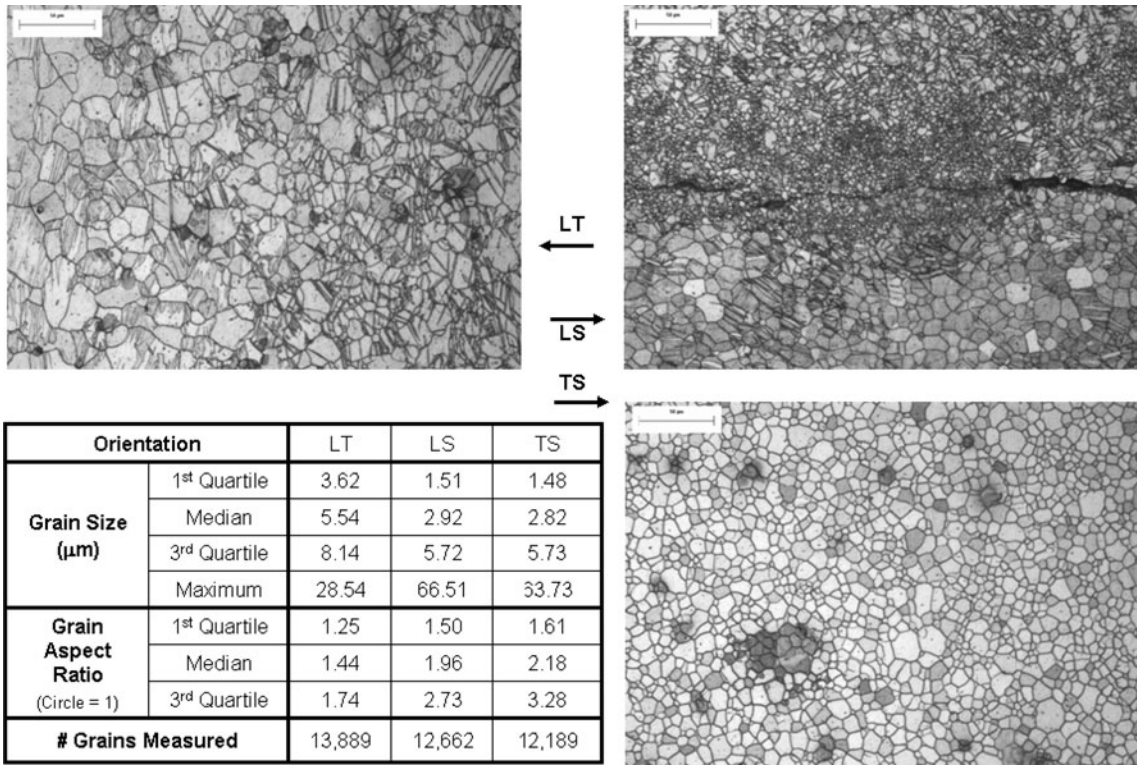

Orientation		LT	LS	TS
Grain Size (μm)	1st Quartile	3.62	1.51	1.48
	Median	5.54	2.92	2.82
	3rd Quartile	8.14	5.72	5.73
	Maximum	28.54	66.51	33.73
Grain Aspect Ratio (Circle = 1)	1st Quartile	1.25	1.50	1.61
	Median	1.44	1.96	2.18
	3rd Quartile	1.74	2.73	3.28
# Grains Measured		13,889	12,662	12,189

Fig. A6 Grain size observed in the CC-2 alloy (heat treated for 15 min at 500 °C)

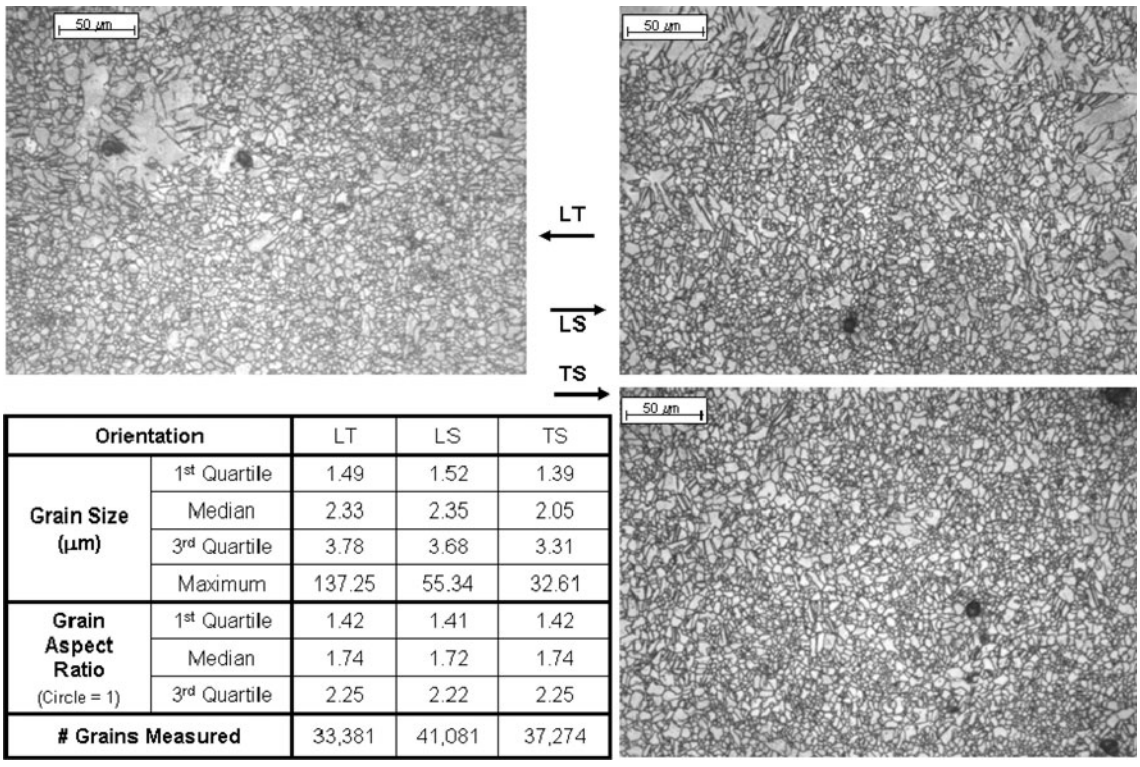

Orientation		LT	LS	TS
Grain Size (μm)	1st Quartile	1.49	1.52	1.39
	Median	2.33	2.35	2.05
	3rd Quartile	3.78	3.68	3.31
	Maximum	137.25	55.34	32.61
Grain Aspect Ratio (Circle = 1)	1st Quartile	1.42	1.41	1.42
	Median	1.74	1.72	1.74
	3rd Quartile	2.25	2.22	2.25
# Grains Measured		33,381	41,081	37,274

Fig. A7 Grain size observed in the CC-3 alloy (as-received condition)

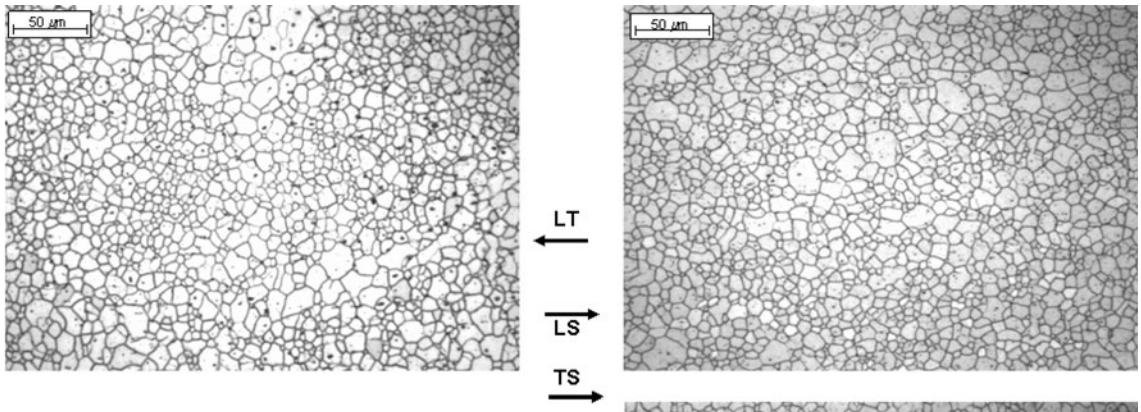

Orientation		LT	LS	TS
Grain Size (μm)	1st Quartile	3.41	4.32	3.97
	Median	5.22	6.25	5.84
	3rd Quartile	7.74	8.87	8.51
	Maximum	45.37	27.71	30.11
Grain Aspect Ratio (Circle = 1)	1st Quartile	1.26	1.26	1.27
	Median	1.45	1.45	1.47
	3rd Quartile	1.72	1.73	1.78
# Grains Measured		14,130	11,027	11,766

Fig. A8 Grain size observed in the CC-3 alloy (heat treated for 15 min at 500 °C)

References

1. B.A. Behrens, G. Kurz, and S. Hübner, Heated Hydro-Mechanical Deep Drawing of Magnesium Sheet Metal, *New Developments in Sheet Metal Forming*, K. Siegert, Ed., Institute for Metal Forming, Technology University of Stuttgart, MAT INFO Werkstoff-Informationsgellschaft mbH, Frankfurt, Germany, 2004, p 379–398
2. W.H. Hunt, and D.R. Herling, Cost Assessment of Emerging Magnesium Sheet Production Methods, Pacific Northwest Laboratories Report PNNL-15368, September 2005
3. P.A. Friedman, The Current State of Aluminum Continuous Casting and its Potential in the Automotive Industry, Internal Ford Technical Report, 1997
4. ASM, *Magnesium and Magnesium Alloys (ASM Specialty Book),* M.M. Avedesian, Ed., ASM International, Materials Park, OH, 1999
5. E.F. Emley, *Principles of Magnesium Technology*, Pergamon Press, New York, NY, 1966
6. P.A. Friedman and A.K. Ghosh, Control of Superplastic Deformation Rate During Uniaxial Tensile Tests, *Metall. Trans.*, 1996, **27A**(10), p 3030–3042
7. P.A. Friedman and W.B. Copple, Superplastic Response in Al-Mg Sheet Alloys, *J. Mater. Eng. Perform.*, 2004, **13**, p 335–347
8. A.K. Ghosh and R. Raj, Grain Size Distribution Effects in Superplasticity, *Acta Metall.*, 1981, **29**, p 607–616
9. G. Cooper, S.G. Luckey, W. Copple, D. Houston, and P.A. Friedman, Superplastic Forming of Magnesium Sheet, *Trans. NAMRI/SME*, 2007, **35**, p 375–382